PHYSICAL REVIEW B **89**, 085401 (2014)

Screening and atomic-scale engineering of the potential at a topological insulator surface

P. Löptien,[1] L. Zhou,[1,*] J. Wiebe,[1] A. A. Khajetoorians,[1] J. L. Mi,[2] B. B. Iversen,[2] Ph. Hofmann,[3] and R. Wiesendanger[1]
[1]*Institute for Applied Physics, Hamburg University, D-20355 Hamburg, Germany*
[2]*Center for Materials Crystallography, Department of Chemistry, Interdisciplinary Nanoscience Center, Aarhus University, 8000 Aarhus C, Denmark*
[3]*Department of Physics and Astronomy, Interdisciplinary Nanoscience Center, Aarhus University, 8000 Aarhus C, Denmark*

(Received 26 June 2013; revised manuscript received 16 January 2014; published 3 February 2014)

The electrostatic behavior of a prototypical three-dimensional topological insulator, $Bi_2Se_3(111)$, is investigated by a scanning tunneling microscopy (STM) study of the distribution of Rb atoms adsorbed on the surface. The positively charged ions are screened by both free electrons residing in the topological surface state as well as band bending induced quantum well states of the conduction band, leading to a surprisingly short screening length. Combining a theoretical description of the potential energy with STM-based atomic manipulation, we demonstrate the ability to create tailored electronic potential landscapes on topological surfaces with atomic-scale control.

DOI: 10.1103/PhysRevB.89.085401 PACS number(s): 73.20.At, 68.37.Ef, 77.22.−d, 79.60.−i

I. INTRODUCTION

Topological insulators (TIs) belong to a unique class of exotic quantum materials hosting Dirac-dispersing charge carriers with helical spin textures at surfaces, which are topologically protected by time-reversal symmetry [1,2]. These so-called topological surface states (TSS) have been predicted to host a variety of novel phenomena, thus making them promising for future generation spintronics and quantum computing applications.

However, harnessing the topological character of these materials requires the ability to gate the TSS to control surface transport, analogous to other two-dimensional (2D) systems [3], and for some of the applications to create a gap at the Dirac point. While extensive effort has been spent on understanding whether magnetism induces a gap at the Dirac point [4–7], surface transport through the TSS is still an experimental challenge. This is due in large part to material quality, poor electron mobility, and proper dielectrics. Impurities near the surface can locally gate the TSS leading to unwanted charge disorder [8–10], which limits charge mobility [11]. More strikingly, previous studies have thoroughly shown that a dilute amount of impurities on the surface can heavily modify the TSS via band bending, which induces additional quantum well states (QWS) [12] at the surface with a Rashba character [13]. These results clearly question if 3D TIs with sufficient mobility can be fabricated and how the application of metallic electrodes will modify charge transport through the TSS.

We use scanning tunneling microscopy (STM) to study the screening behavior produced by positively charged Rb atoms on the surface of the prototypical TI Bi_2Se_3. By analyzing the pair correlation functions [14–16], the screened Coulomb potential between surface Rb atoms is extracted, from which the electrostatic properties of the TI are determined. By varying the surface and bulk doping, we show that the charge screening is mainly provided by 2D electrons, residing in both the TSS and the QWS, resulting in a surprisingly small screening length. With that knowledge, we demonstrate the ability to engineer the potential landscape, in which the TSS resides, by atomic manipulation of single Rb atoms on the surface.

II. EXPERIMENTAL METHODS

Both stoichiometric and Ca-doped Bi_2Se_3 single crystals were grown and characterized as described in Refs. [12,17]. Stoichiometric samples are highly n-doped resulting from bulk defects, while Ca doping shifts the Dirac point to lie within 50 meV of the Fermi energy [17]. All experiments were conducted under ultrahigh vacuum conditions with a base pressure below 2×10^{-10} mbar. The crystals were cleaved *in situ* at room temperature exposing the (111) surface. Rubidium was subsequently deposited at room temperature from a commercial dispenser. After deposition, the samples were immediately quenched to low temperatures within the microscope, where STM experiments were performed at $T = 4.3$ K [17]. STM topographs were recorded in constant-current mode, with a tunneling current $I_T = 10$ pA and a sample bias voltage $V_B = 1$ V. The Rb coverage was varied between 0.6% to 7.3% of a monolayer (ML), where a full ML corresponds to a coverage with Rb atoms of equal number as surface Se atoms. With these sample preparation conditions, Rb atoms remain on the surface and do not intercalate as previously demonstrated, where the electronic properties of Rb-covered Bi_2Se_3 as a function of annealing were characterized on the same Bi_2Se_3 crystals used here [17].

III. EXPERIMENTAL RESULTS

STM images of dilutely covered surfaces reveal a distribution of single Rb atoms. These appear as circular protrusions with an apparent height of $\Delta z \approx 150$ pm [Fig. 1(a)]. In Fig. 2(a), an STM topograph of Rb atoms adsorbed on Bi_2Se_3 with atomic resolution of the underlying Bi_2Se_3 substrate is shown. The individual maxima visible on the substrate occur at the positions of the Se atoms in the surface layer [18]. The hexagonal symmetry can be compared to a top view on three unit cells of Bi_2Se_3, depicted in Fig. 2(b). Due to the positions of the Bi and Se subsurface atoms, two

---

[*] lzhou@physnet.uni-hamburg.de

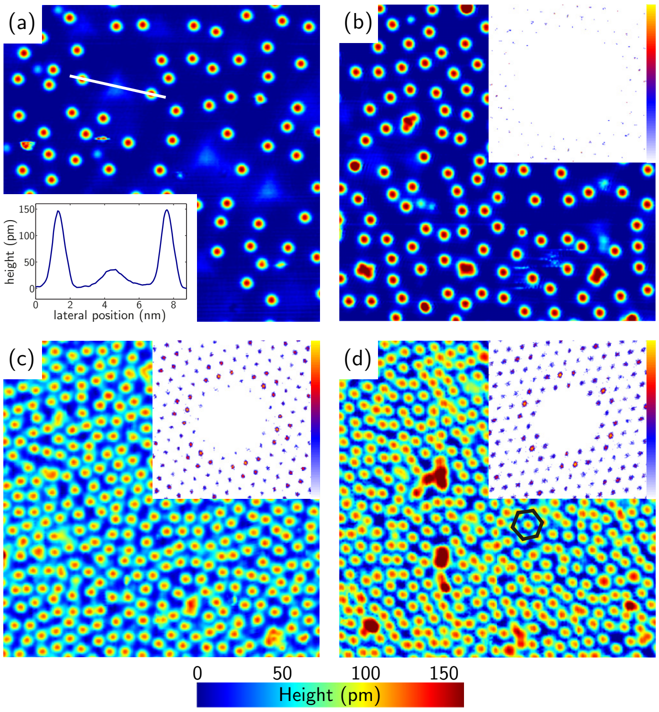

FIG. 1. (Color online) STM topographs of Rb single atoms on stoichiometric and Ca-doped Bi_2Se_3 (30 nm × 30 nm). (a) Stoichiometric Bi_2Se_3 with a 1.2% ML coverage of Rb. The inset indicates a cross section along the line in (a) that depicts the apparent heights of a Se vacancy and two Rb atoms. (b) Ca-doped Bi_2Se_3 with 2.0% ML Rb. (c) Stoichiometric Bi_2Se_3 with 5.8% ML Rb. (d) Stoichiometric Bi_2Se_3 with 6.9% ML Rb. The small hexagon depicts the $(\sqrt{12} \times \sqrt{12})\,R30^\circ$ superstructure. Insets in (b)–(d): autocorrelation plots of the atoms' positions (5 nm × 5 nm, each vector starts at the center. The number of the individual counts is plotted logarithmically using the depicted color scale).

nonequivalent, threefold coordinated, hollow binding sites for the Rb adatoms exist. In Fig. 2(a), straight lines have been drawn along the positions of the Se surface atoms. As depicted by these lines, the Rb atoms bind at only one of the two possible binding sites. However, from the STM measurements alone, without any input by, e.g., *ab initio* calculations, it remains unclear which particular site is preferred, but this is unimportant for the further data analysis. In addition to the Rb atoms, Se subsurface vacancies appear in Fig. 1(a) as extended triangular shapes with $\Delta z \approx 30$ pm, depending on the depth of the vacancy [18]. A strongly reduced density of Rb atoms in the vicinity of these positively charged Se vacancies, together with the observation that Rb atoms do not cluster, indicates the positive charge of single Rb atoms on the surface [17,19]. From topographs of the pristine surface with a total area of ≈50 000 nm^2, we estimate the surface density of Se vacancies and Ca acceptors to be one to two orders of magnitude smaller than the surface density of Rb atoms. We therefore neglect their effect on the distribution of Rb atoms on the surface.

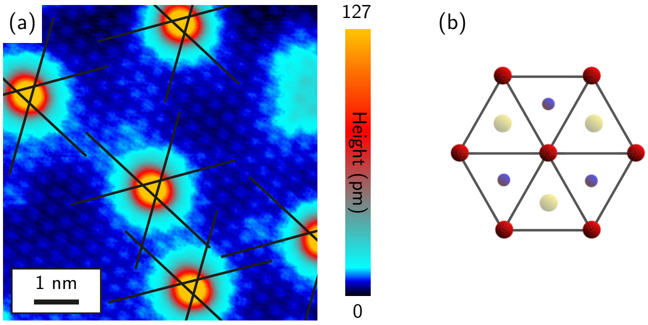

FIG. 2. (Color online) (a) STM topograph of Rb adatoms on an intrinsic Bi_2Se_3 sample, with atomic resolution of the substrate lattice. (b) Top view on three unit cells of the $Bi_2Se_3(111)$ surface, cleaved along the van der Waals gap. The surface Se atoms are colored red, the subsurface Bi atoms are blue, and the second subsurface Se atoms are yellow.

Images with a higher coverage of Rb atoms [Figs. 1(b)–1(d)] reveal a very homogeneous, highly nonrandomized distribution of Rb atoms across the surface. In certain regions, ordered superlattice arrays of Rb with a $(\sqrt{12} \times \sqrt{12})\,R30^\circ$ structure can be clearly observed when the Rb coverage is sufficiently high [small hexagon in Figs. 1(d) and 5(a)]. Such ordering of impurities on surfaces has been attributed to various substrate-mediated electronic interactions [15,16,20]. The positive charge of Rb on the surface suggests that this ordering is driven by a repulsive Coulombic interaction between Rb atoms. Moreover, the observation of such ordering indicates that upon deposition, the thermal energy is sufficient for the system to equilibrate.

The autocorrelations of the coverage-dependent distributions of Rb are determined as described in Appendix A1. The autocorrelation images [Figs. 1(b)–1(d)] illustrate the displacement of all surrounding atoms with respect to a given atom, for all atoms in the image. These images reveal a hexagonal distribution of Rb atoms, which again reflects the underlying symmetry of the substrate surface lattice. Moreover, these images reveal a radius of $r \approx 1$ nm around every Rb atom at which no other Rb atoms reside.

IV. STATISTICAL ANALYSIS

To quantify this effect and relate it to the underlying potential landscape, we performed a statistical analysis of each Rb atom and its neighbors. Since the autocorrelation images reveal a noncircular symmetric distribution, we consider a vector-resolved analysis of the displacement of each Rb atom relative to its neighbors [21]. In total, the coordinates of >20 000 atoms on an area of 280 nm × 280 nm were determined from STM topographs. We define individual bins represented by hexagonal unit cells that resemble the allowed binding sites. All unit cells at a given distance are indexed by the same parameter j, while the parameter k distinguishes the different positions for a given j. For a given autocorrelation image, we count the number of atoms in a given unit cell [Fig. 3(a)].

There, the highest peaks are observed for cells where $j = 6$ (purple), which corresponds to the $(\sqrt{12} \times \sqrt{12})\,R30^\circ$ superstructure and indicates that Rb atoms have the highest probable interatomic distances of $r = 1.43$ nm. The subsequent local maxima, namely for $j = 15,19$ (green, gray), have the same displacement from cells where $j = 6$, as cells with $j = 6$

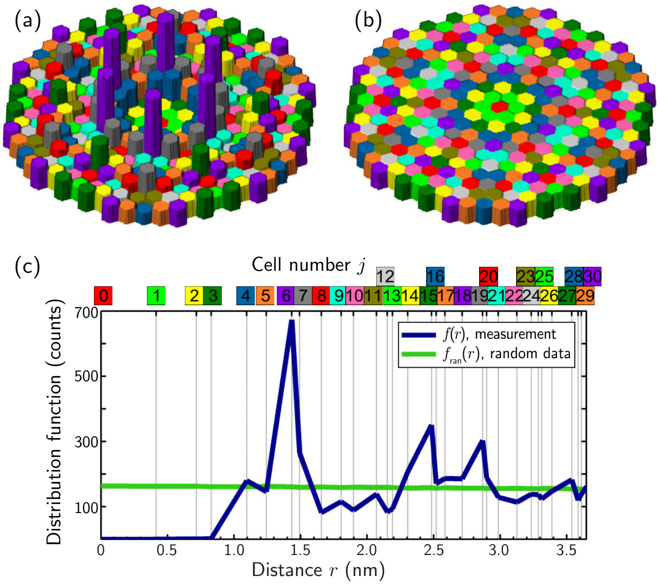

FIG. 3. (Color online) (a) The counts, represented by height, from the autocorrelation images are indexed into colored hexagonal cells labeled by (j,k), shown here for the coverage in Fig. 1(d). (b) Same procedure for a randomly generated distribution with the same coverage. (c) Distribution functions $f(r)$ and $f_{\mathrm{ran}}(r)$ extracted from (a) and (b), respectively, after averaging over all k values for a given j. Each hexagonal cell j is color-coded in (a) and (b) as indicated above the graph.

have from the origin. This further indicates the long-range nature of the Rb-Rb interaction. Upon closer inspection, the experimental distribution is found to be symmetric, namely, independent of the index k, thereby allowing all cells with a given j to be averaged over all k. The resultant coverage- and distance-dependent distribution function $f(r)$, which counts the number of Rb atoms at a given distance from any Rb atom, is graphed in Fig. 3(c). While $f(r)$ reveals information about the potential landscape, it is coverage dependent and needs to be normalized to a random distribution function, $f_{\mathrm{ran}}(r)$, with the same coverage [Figs. 3(b) and 3(c)]. The underlying details are described in Appendix A2. The ratio between both distribution functions yields the pair correlation function $g(r) = f(r)/f_{\mathrm{ran}}(r)$, which represents the potential of mean force $w(r)$, namely, the work required to pull two Rb atoms from infinite distance to a distance r [14]:

$$-\ln g(r) = w(r)/k_{\mathrm{B}}T = [v(r) + \Delta w(r)]/k_{\mathrm{B}}T\ . \qquad (1)$$

Here, $w(r)$ can be separated into two terms, namely, a pairwise term called the pair potential $v(r)$ and a higher-order term $\Delta w(r)$. While $v(r)$ equals $w(r)$ in a dilute range, for higher coverage higher-order neighbors affect the distribution of atoms, and an indirect correlation term needs to be taken into account. The separation of $g(r)$ into a direct and indirect correlation terms is known in the theory of fluids as the Ornstein-Zernike relation [22] and can be solved using the Percus-Yevick approximation [14,23]. As it is described in more detail in Appendix A3, a self-consistent determination returns $v(r)$ between pairs of atoms as the quantity of interest.

In Fig. 4(a), the reduced pair potential $v(r)/k_{\mathrm{B}}T$ is plotted for different surface coverages and different bulk dopings.

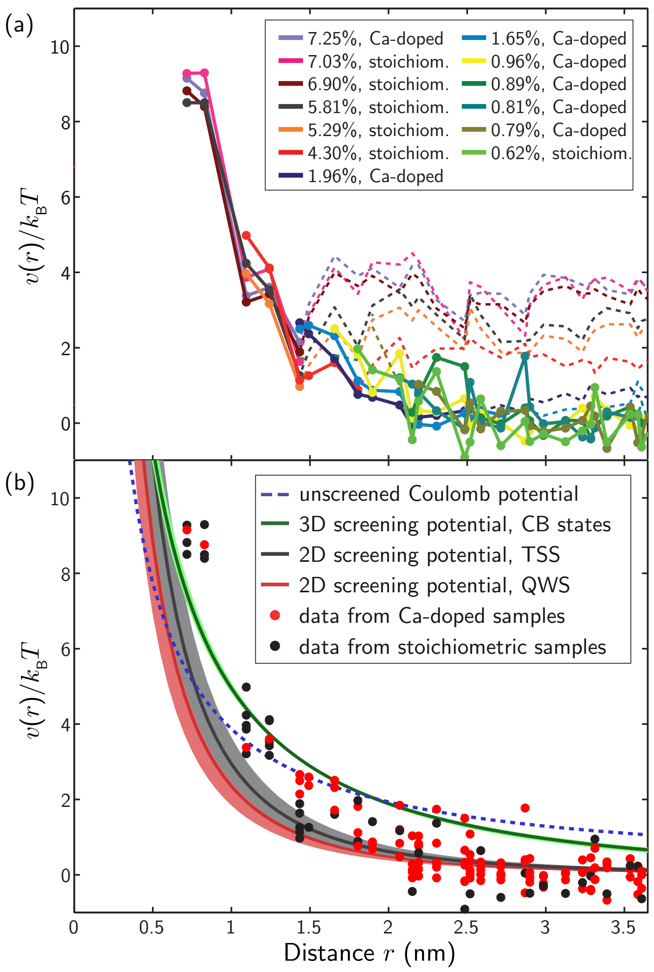

FIG. 4. (Color online) (a) Reduced pair potential, $v(r)/k_{\mathrm{B}}T$, for various Rb coverages and for stoichiometric and Ca-doped $\mathrm{Bi_2Se_3}$. The lines connect points at a given coverage as a guide to the eye. The dashed lines mark regions where $v(r)/k_{\mathrm{B}}T$ is affected by a limitation of the Percus-Yevick approximation. (b) The experimental data from (a), taking only the data points into account, which are connected by solid lines, are fitted with different unscreened and screened Coulomb potentials, where the shaded regions indicate the error bars (see text).

As indicated in Fig. 1, short separations are forbidden and $v(r)$ curves start at r considerably larger than 0. For small distances, $v(r)$ decreases monotonically regardless of coverage. However, for larger r, there is an increase in $v(r)$ for higher coverage due to the influence of higher-order neighbors in $w(r)$. This is an artifact in $v(r)$ due to the breakdown of the Percus-Yevick approximation of $\Delta w(r)$ at larger distances (Appendix A3). Hence the tails of the $v(r)$ curves for the higher coverages that do not asymptotically approach zero [dashed lines in Fig. 4(a)] are not considered for the further analysis.

V. CHARGE SCREENING

To extract the potential landscape responsible for the repulsive interaction between neighboring charged atoms, we fitted $v(r)/k_{\mathrm{B}}T$ to various types of Coulomb potentials [Fig. 4(b)]. Immediately, an unscreened Coulomb potential, where the dielectric constant ε_r is the sole free parameter, can be excluded. The experimental data decay much faster than the fitted function. Therefore we consider a screened Coulomb potential where free electrons can screen the charged atoms. The screening electrons can originate from three sources: (i) bulk states, (ii) band-bending induced QWS in the conduction band [17], and (iii) TSS. In the following, we distinguish between the screening effects resulting from these three different sources within the Thomas-Fermi theory of screening.

The bulk-related screening can be readily ruled out. Because the positively charged Rb atoms can be screened only by negative charges, one would expect a significantly larger screening length for Ca-doped (p-doped) $\mathrm{Bi_2Se_3}$ than for stoichiometric (degenerately n-doped) $\mathrm{Bi_2Se_3}$ if there would be a decisive bulk-related screening. This effect is not observed experimentally, i.e., the data show no dependence on the bulk doping [Fig. 4(a)]. Nevertheless, we try to fit the data to a bulk-screening model

$$v_{3\mathrm{D}}(r) = \frac{e^2}{4\pi\varepsilon_0(\varepsilon_r+1)/2}\frac{1}{r}\,\mathrm{e}^{-r/R_{3\mathrm{D}}}\,, \tag{2}$$

with the screening length [24,25]

$$R_{3\mathrm{D}} = \sqrt{\frac{\varepsilon_0\varepsilon_r}{e^2\,\partial n/\partial\mu}}\,. \tag{3}$$

We consider that each Rb atom has a charge of one full electron [17,19]. $\partial n/\partial\mu$ is related to the density of states at E_F, assuming a typical parabolic dispersion for a 3D system [25]. The value of E_F was taken from ARPES measurements of stoichiometric samples [26], and the effective mass m^* from Ref. [27] was used here. ε_r is used as the only fitting parameter, yielding $\varepsilon_r^{3\mathrm{D}} = (16.2 \pm 1.3)$ and $R_{3\mathrm{D}} = (3.70 \pm 0.61)$ nm. This value of $\varepsilon_r^{3\mathrm{D}}$ is unreasonably smaller than the well-characterized and well-accepted bulk value of 113 [28]. Moreover, the fitted 3D potential in Fig. 4(b) (green curve) decays slower than the experimental data and poorly fits the data. Clearly, all these observations lead to the conclusion that the bulk-related screening is not decisive in the screening of Rb atoms at the surface, rendering the surface free electrons responsible for the screening potential.

To quantify the 2D potential produced by surface-related free electrons originating from those occupying the QWS and the TSS, we utilize the following form of the potential [24,25], which represents the situation of a 2D conductive sheet on a bulk dielectric with a dielectric constant of ε_r,

$$v_{2\mathrm{D}}(r) = \frac{e^2}{4\pi\varepsilon_0(\varepsilon_r+1)/2}\frac{1}{r}\left[1 - \frac{\pi}{2}\xi(H_0(\xi) - N_0(\xi))\right] \tag{4}$$

with $\xi = r/R_{2\mathrm{D}}$, H_0 and N_0 the Struve and Neumann functions, respectively, and the screening length

$$R_{2\mathrm{D}} = \frac{\varepsilon_0(\varepsilon_r+1)}{e^2\,\partial n/\partial\mu}\,. \tag{5}$$

To exemplify the role of both electron types on the screening, we only consider the limiting cases where the screening is done solely by either the QWS or the TSS electrons. $\partial n/\partial\mu$ is calculated assuming a parabolic 2D dispersion [25] in case of the QWS,

$$\frac{\partial n}{\partial\mu} = \frac{m^*}{\pi\hbar^2\,[\exp(-E_\mathrm{F}/k_\mathrm{B}T)+1]}\,, \tag{6}$$

and a linear dispersion, $E = \hbar v_\mathrm{F} k = Ak$ [29], in the case of the TSS,

$$\frac{\partial n}{\partial\mu} = \frac{k_\mathrm{F}}{2\pi\,A}\,. \tag{7}$$

For the whole range of Rb coverage, we assume that (i) the charge transfer per Rb atom is always one electron and (ii) the surface band bending that determines $\partial n/\partial\mu$ is constant. From the ARPES measurements of the Rb-induced surface band bending of Ref. [19], we estimate that (i) is strictly valid for coverages up to about 4%. At our highest coverages, the charging probability of each Rb atom might go slightly down due to Coulomb interaction with neighboring atoms according to the surface doping model [30]. Therefore the carrier densities in the TSS and QWS together only vary between 5×10^{12} cm^{-2} (0.6% ML Rb) and 3×10^{13} cm^{-2} (7.3% ML Rb). Regarding (ii), at the coverages we used, the surface band bending is close to saturation, and varies by at most 50% within the low-coverage range [19]. Therefore the parameters that enter the 2D models [Eqs. (4)–(7)] have the following variations. In case of the QWS, the deviations from a parabolic dispersion lead to $m^* = (0.15 \pm 0.04)\,m_e$. There is no further effect of the amount of band bending, since the actual E_F that enters Eq. (6) is always well above $k_\mathrm{B}T$. For the TSS, the variation of band bending leads to $k_\mathrm{F} = (0.13 \pm 0.03)$ Å^{-1} and $A = (4.06 \pm 0.05)$ eVÅ. All these values were derived from ARPES measurements that were published in Ref. [17].

In Fig. 4(b), both 2D potentials have been fitted to the experimental data considering the above variations in the parameters through their error bars, and using ε_r as only fitting parameter (red and black curve with shaded regions indicating errors), yielding $\varepsilon_r^{\mathrm{QWS}} = (6.8 \pm 2.4)$ and $R_{2\mathrm{D}}^{\mathrm{QWS}} = (0.66 \pm 0.01)$ nm for the QWS, and $\varepsilon_r^{\mathrm{TSS}} = (5.2 \pm 1.2)$ and $R_{2\mathrm{D}}^{\mathrm{TSS}} = (0.66 \pm 0.01)$ nm for the TSS, respectively. The two curves are in better agreement with the experimental data than the bulk screening model. In particular, the decay of each fit better recounts the experimental behavior. However, the experimental data indicate less effective screening than both 2D models for the short-distance range, which corresponds to rather high Rb coverages. In order to rule out that a deviation from the above assumptions (i) and (ii) for the used parameters leads to an error in the determined screening length, we fitted the 2D screening models to the different subsets of the data in Fig. 4(a) with almost constant Rb coverage, resulting in a variation of ε_r and $R_{2\mathrm{D}}$ by less than 50%. Therefore the unexpectedly short fitted value of $R_{2\mathrm{D}}$ is reliable, and results from the very small ε_r as compared to literature values ranging from 30 to 113 [8,28]. The small value of ε_r obtained in the fit implies that the QWS and TSS electrons that dominate the screening behave almost like electrons of a freestanding 2D conducting surface in vacuum [24].

In the following, we discuss the remaining possible reasons for the short-distance deviations of the 2D screening models from the experimental data. We considered the effect of each screening process individually, in each fit. In reality, all screening potentials contribute to the observed Rb distribution, which may account for deviations in the fits when compared to the experimental data. However, in the short-distance range, the data indicate a *less* efficient screening than each of the individual screening models, which rules out that this effect can explain the short-range deviations. Finally, deficiencies of the used Thomas-Fermi screening theory, which might fail in the short-distance range, could be responsible for these deviations. Alternative descriptions of the screening, e.g., via random phase approximation [9], would be further complicated by the Rashba splitting of the QWS [13], which would have a marked effect, because it prevents direct backscattering similar to the TSS. This more complex description is beyond the scope of the current work.

VI. ENGINEERING OF POTENTIAL LANDSCAPES

In the remaining part of this publication, we examine methods to controllably engineer the potential landscape, in which the TSS electrons reside, via the manipulation of the Rb distribution. In addition to self-assembly of Rb atoms driven by the underlying screening potential, we demonstrate it is possible to atomically manipulate individual Rb atoms on the surface of the topological insulator. Figures 5(a) and 5(b) illustrate first the self-assembly of Rb atoms into an ordered array and subsequent manipulation of Rb atoms into the shape of a corral with the STM tip [31]. By combining the ability to do atomic engineering with charged impurities, with the knowledge of the 2D potential landscape, it is possible to tailor a particular energy landscape at the topological surface while simultaneously predicting the resultant 2D electrostatic potential [Fig. 5(c)]. Using this technique, patches of a locally high homogeneous Rb coverage on a Rb-free area of the surface can be assembled. For a Ca-doped substrate, where the TSS is unoccupied without Rb coverage but occupied below the Rb-patch, this results in a quantum confinement of the Dirac electrons [32] of the TSS, which can be tailored by the size and shape of the patch in a very controlled fashion.

VII. SUMMARY

In summary, we have mapped the screened Coulomb potential on a topological surface driven by charged Rb atoms. Our observations reveal that screening of surface electrons at $Bi_2Se_3(111)$ is surprisingly efficient as manifested by a short screening length. While the charge screening here is an interplay between different screening potentials, the role of the TSS on charge screening could be further understood by comparing these results with complementary studies of alkali atom distributions on other prototypical TI systems like Bi_2Se_2Te or Bi_2Te_3 where the Fermi surface is different compared to Bi_2Se_3. Combining the electrostatic screening around the charged impurities and the ability to perform atomic-scale manipulation, we have demonstrated the ability to engineer the potential landscape at the surface of a topological insulator.

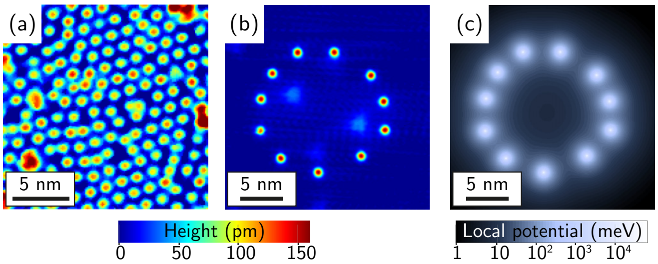

FIG. 5. (Color online) Tailoring the local potential by surface doping with Rb atoms. (a) Self-assembly of Rb atoms into a superlattice array driven by Coulomb repulsion. (b) Eleven Rb atoms manipulated with the STM tip. The triangles in the center of the "corral" are native subsurface Se vacancies. Manipulation parameters are $I_T = 4.6$ nA and $V_B = 600$ mV. (c) Potential landscapes of (b) generated by using $v_{2D}(r)$.

ACKNOWLEDGMENTS

We acknowledge financial support from the DFG via SFB 668, Graduiertenkolleg 1286, and SPP 1666, from the ERC Advanced Grant "FURORE," from the VILLUM foundation, and from the Danish National Research Foundation. A.A.K. acknowledges Project No. KH324/1-1 from the Emmy–Noether-Program of the DFG.

APPENDIX: STATISTICAL DATA ANALYSIS

1. Autocorrelation functions

Autocorrelation functions $a(\boldsymbol{r})$ of the positions $\boldsymbol{r}_i$ of atoms are calculated by taking the combinations between all N atoms inside a particular area into account:

$$a(\boldsymbol{r}) = \sum_{i=1}^{N} \sum_{\substack{j=1 \\ j \neq i}}^{N} \delta_{\boldsymbol{r}\boldsymbol{r}'} \quad \text{with} \quad \boldsymbol{r}' = \boldsymbol{r}_i - \boldsymbol{r}_j. \tag{A1}$$

This formula takes all combinations of atoms into account twice and returns $N(N-1)$ combinations in total. Typically, this evaluation is performed on areas of (60×60) nm^2, leading to $\sqrt{2} \times 60$ nm as a maximum distance in $a(\boldsymbol{r})$. The insets of Fig. 1 depict the central (5×5) nm^2 areas of the autocorrelation functions $a(\boldsymbol{r})$, with $\boldsymbol{r} = 0$ located in the center.

2. Random distribution functions

The random distribution function $f_{\mathrm{ran}}(j,k)$ is obtained from random distributions of Rb atoms. These are generated by using an algorithm that returns uniformly distributed pseudorandom numbers, where the number N and the area is the same as in the experimental $f(j,k)$. Accordingly, $f_{\mathrm{ran}}(j,k)$ is extracted by the same data evaluation technique. An average of 40 generated random distribution functions is used. As it is indicated in Fig. 3(b), the statistical base of typically 90×10^6 pairs (for the case of an ensemble with 1500 atoms) results in a very flat distribution that is rather independent of j and k.

3. Indirect correlation effects

The theory about the pair correlation function $g(\boldsymbol{r})$ and its connection to the potential of mean force $w(\boldsymbol{r})$ is explained in several textbooks about statistical mechanics of liquids and fluids [14]. As expressed by Eq. (1), the work required to pull two particles close together, $w(\boldsymbol{r})$, depends not only on the pair potential $v(\mathbf{r})$ between pairs of particles, but also on a term due to the surrounding particles in the system, denoted by $\Delta w(\mathbf{r})$.

Likewise, the correlation between two atoms can be split in a direct correlation and an indirect one, that is mediated by a third atom or even higher orders. This indirect correlation effect is expressed by the Ornstein-Zernike relation [14,22]:

$$g(\mathbf{r}) - 1 = c(\mathbf{r}) + \rho \int c(\mathbf{r}')\,[g(|\mathbf{r}-\mathbf{r}'|) - 1]\,\mathrm{d}\mathbf{r}'. \tag{A2}$$

It needs to be solved by an approximate closure equation. Here, we use the Percus-Yevick approximation [23], leading to the following expression [14], where ρ and β denote the average number density and the inverse temperature $\beta = 1/k_\mathrm{B}T$, respectively:

$$e^{\beta v(\mathbf{r})}\,g(\mathbf{r}) = 1 + \rho \int [g(\mathbf{r}-\mathbf{r}') - 1][1 - e^{\beta v(\mathbf{r}')}]g(\mathbf{r}')\,\mathrm{d}\mathbf{r}'. \tag{A3}$$

According to Eq. (1), the logarithm of the Percus-Yevick equation equals $-\beta\Delta w(\mathbf{r})$. It is calculated by a summation over the hexagonal cells that are used as the basis for $g(\mathbf{r})$ (see Fig. 3 for comparison). Experimental data for cell numbers up to 20 are taken into account. For higher distances, the uncorrelated limit $g \rightarrow 1$ is used. The cells have degeneracies of either 1, 6, 12, or 18:

$$-\beta\Delta w(\mathbf{r}) = \ln\left[1 + \rho \sum_{i=0}^{20} \sum_{k=1}^{\text{degeneracy}} [g(\mathbf{r}(j) - \mathbf{r}(i,k)) - 1] \times \{1 - \exp[\beta v(\mathbf{r}(i,k))]\}g(\mathbf{r}(i,k))\right]. \tag{A4}$$

This equation needs to be solved self-consistently using the experimentally derived $g(\mathbf{r})$ from various data sets and assumed forms for the pair potential, named, $v_\mathrm{PY}(\mathbf{r})$. Because of the observed symmetry in $g(r)$, namely, its independence on the angular index k, the pair potential depends only on the relative separation r. Without any loss of generality, a Yukawa form for $v_\mathrm{PY}(r)$ is used, because it fits well to any physically possible pair potential:

$$v_\mathrm{PY}(r) = \frac{1}{4\pi\varepsilon_0(\varepsilon_{r,\mathrm{PY}}+1)/2}\,\frac{e^2}{r}\,\mathrm{e}^{-r/\lambda_\mathrm{PY}}. \tag{A5}$$

In the limit $\lambda_\mathrm{PY} \rightarrow \infty$, it reduces to an unscreened Coulomb potential. A 3D screening potential $v_\mathrm{3D}(r)$ has exactly the Yukawa form, and even a 2D screening potential $v_\mathrm{2D}(r)$ fits well to a Yukawa form when using different parameters [25]. Depending on the two free parameters $(\varepsilon_{r,\mathrm{PY}}+1)/2$ and λ_PY, which are varied within a certain range, Eq. (A4) is calculated. The aim is to minimize the deviation between its left- and right-hand sides. Squared deviations for the individual data points are summed up and normalized. This average deviation is plotted color-coded as a function of $(\varepsilon_{r,\mathrm{PY}}+1)/2$ and λ_PY in Fig. 6(a). It is found that an unscreened Coulomb potential $v_\mathrm{PY}(r)$ is not in accordance with the Percus-Yevick equation, because going towards the limit of an infinite λ_PY the deviation always rises. The optimal parameters to solve Eq. (A4) self-consistently are constricted to a narrow range around $(\varepsilon_{r,\mathrm{PY}}+1)/2 = 3.6^{+1.2}_{-1.0}$ and $\lambda_\mathrm{PY} = 1.0^{+0.4}_{-0.4}$ nm. Data sets from both Ca-doped and intrinsic samples have been treated independent at first, but during the analysis, it was found that they can be described by the very same form of $v_\mathrm{PY}(r)$. The used data points are all taken from the range of r up to the global maximum of $f(r)$ (compare to Fig. 3). For higher distances, the Percus-Yevick approximation gives unphysical imaginary numbers, but that region is not of interest. When comparing values of $-\Delta w(r)/k_\mathrm{B}T$ from one data set, but for different distances r within the range of interest, the relative standard deviation of these values is only up to ≈7%. This is not unexpected, because the Helmholtz free energy of the system of surrounding particles should stay relatively constant when no additional particles are added and just two particles change their relative separation on that small scale. In contrast, it should change severely when additional particles are added. This is in accordance with the experimental results, where Δw differs in between the data sets with different Rb coverages. In the following, the average of $\Delta w(r)$ over r is used and Δw becomes a function of only the Rb coverage. In Fig. 6(b), the data points for $-\Delta w(N)/k_\mathrm{B}T$ reflect the individual data sets with different coverages that are also used in Fig. 6(a). The solid line is a fit to a function that is quadratic in N. With $\Delta w(N)$ being determined, it is now possible to extract $v(r)$ from $w(r)$.

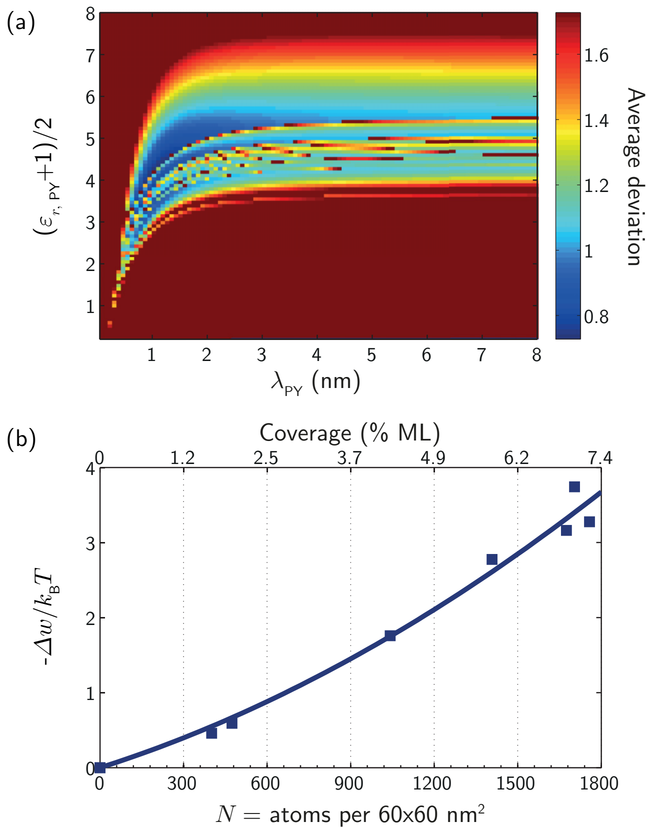

FIG. 6. (Color online) (a) The optimum $v_\mathrm{PY}(r)$ is determined by varying the parameters $(\varepsilon_{r,\mathrm{PY}}+1)/2$ and λ_PY. For all combinations, squared deviations between the left- and right-hand sides of the Percus-Yevick equation are plotted color-coded. (b) Plot of the coverage-dependent right-hand side of the Percus-Yevick equation that equals $-\Delta w(N)/k_\mathrm{B}T$. The solid line is a fit to a function, which is quadratic in N.

[1] M. Hasan and C. Kane, Rev. Mod. Phys. **82**, 3045 (2010).
[2] X.-L. Qi and S.-C. Zhang, Rev. Mod. Phys. **83**, 1057 (2011).
[3] R. Balog *et al.*, Nat. Mater. **9**, 315 (2010).
[4] L. A. Wray, S.-Y. Xu, Y. Xia, D. Hsieh, A. V. Fedorov, Y. S. Hor, R. J. Cava, A. Bansil, H. Lin, and M. Z. Hasan, Nat. Phys. **7**, 32 (2011).
[5] J. Honolka *et al.*, Phys. Rev. Lett. **108**, 256811 (2012).
[6] R. R. Biswas and A. V. Balatsky, Phys. Rev. B **81**, 233405 (2010).
[7] T. Schlenk *et al.*, Phys. Rev. Lett. **110**, 126804 (2013).
[8] H. Beidenkopf, P. Roushan, J. Seo, L. Gorman, I. Drozdov, Y. S. Hor, R. J. Cava, and A. Yazdani, Nat. Phys. **7**, 939 (2011).
[9] S. Adam, E. H. Hwang, and S. Das Sarma, Phys. Rev. B **85**, 235413 (2012).
[10] C. Mann, D. West, I. Miotkowski, Y. P. Chen, S. Zhang, and C.-K. Shih, Nat. Commun. **4**, 2277 (2013).
[11] D. Kim, S. Cho, N. P. Butch, P. Syers, K. Kirshenbaum, S. Adam, J. Paglione, and M. S. Fuhrer, Nat. Phys. **8**, 459 (2012).
[12] M. Bianchi, D. Guan, S. Bao, J. Mi, B. B. Iversen, P. D. C. King, and P. Hofmann, Nat. Commun. **1**, 128 (2010).
[13] P. D. C. King *et al.*, Phys. Rev. Lett. **107**, 096802 (2011).
[14] J. P. Hansen, *Theory of Simple Liquids* (Academic Press, London, 1976); T. L. Hill, *Statistical Mechanics* (McGraw-Hill, New York, 1956); D. Chandler, *Introduction to Modern Statistical Mechanics* (Oxford University Press, New York, 1987).
[15] I. Fernandez-Torrente, S. Monturet, K. J. Franke, J. Fraxedas, N. Lorente, and J. I. Pascual, Phys. Rev. Lett. **99**, 176103 (2007).
[16] C.-L. Song, B. Sun, Y.-L. Wang, Y.-P. Jiang, L. Wang, K. He, X. Chen, P. Zhang, X.-C. Ma, and Q.-K. Xue, Phys. Rev. Lett. **108**, 156803 (2012).
[17] M. Bianchi, R. C. Hatch, Z. Li, P. Hofmann, F. Song, J. Mi, B. B. Iversen, Z. M. Abd El-Fattah, P. Löptien, L. Zhou, A. A. Khajetoorians, J. Wiebe, R. Wiesendanger, and J. W. Wells, ACS Nano **6**, 7009 (2012).
[18] S. Urazhdin, D. Bilc, S. H. Tessmer, S. D. Mahanti, T. Kyratsi, and M. G. Kanatzidis, Phys. Rev. B **66**, 161306 (2002); S. Urazhdin, D. Bilc, S. D. Mahanti, S. H. Tessmer, T. Kyratsi, and M. G. Kanatzidis, *ibid.* **69**, 085313 (2004).
[19] T. Valla, Z.-H. Pan, D. Gardner, Y. S. Lee, and S. Chu, Phys. Rev. Lett. **108**, 117601 (2012).
[20] F. Silly, M. Pivetta, M. Ternes, F. Patthey, J. P. Pelz, and W.-D. Schneider, Phys. Rev. Lett. **92**, 016101 (2004).
[21] J. Trost, T. Zambelli, J. Wintterlin, and G. Ertl, Phys. Rev. B **54**, 17850 (1996).
[22] L. S. Ornstein and F. Zernike, Proc. Acad. Sci. Amsterdam **17**, 793 (1914).
[23] J. Percus and G. Yevick, Phys. Rev. **110**, 1 (1958).
[24] M. R. Krčmar, W. M. Saslow, and M. B. Weimer, Phys. Rev. B **61**, 13821 (2000); M. R. Krčmar and W. M. Saslow, *ibid.* **66**, 235310 (2002).
[25] A. Laubsch, K. Urban, and Ph. Ebert, Phys. Rev. B **80**, 245314 (2009).
[26] M. Bianchi, R. C. Hatch, D. Guan, T. Planke, J. Mi, B. B. Iversen, and P. Hofmann, Semicond. Sci. Technol. **27**, 124001 (2012).
[27] H. Köhler, Phys. Status Solidi (B) **58**, 91 (1973).
[28] W. Richter, H. Köhler, and C. R. Becker, Phys. Status Solidi (B) **84**, 619 (1977).
[29] D. Culcer, E. H. Hwang, T. D. Stanescu, and S. Das Sarma, Phys. Rev. B **82**, 155457 (2010).
[30] M. Morgenstern, M. Getzlaff, D. Haude, R. Wiesendanger, and R. L. Johnson, Phys. Rev. B **61**, 13805 (2000).
[31] M. F. Crommie, C. P. Lutz, and D. M. Eigler, Science **262**, 218 (1993).
[32] S. K. Hämäläinen, Z. Sun, M. P. Boneschanscher, A. Uppstu, M. Ijäs, A. Harju, D. Vanmaekelbergh, and P. Liljeroth, Phys. Rev. Lett. **107**, 236803 (2011).